JACS
JOURNAL OF THE AMERICAN CHEMICAL SOCIETY

Article

pubs.acs.org/JACS

Periodic Trends in Olefin Epoxidation over Group IV and V Framework-Substituted Zeolite Catalysts: A Kinetic and Spectroscopic Study

Daniel T. Bregante and David W. Flaherty*

Department of Chemical and Biomolecular Engineering, University of Illinois at Urbana−Champaign, Urbana, Illinois 61801, United States

Supporting Information

ABSTRACT: Group IV and V framework-substituted zeolites have been used for olefin epoxidation reactions for decades, yet the underlying properties that determine the selectivities and turnover rates of these catalysts have not yet been elucidated. Here, a combination of kinetic, thermodynamic, and in situ spectroscopic measurements show that when group IV (i.e., Ti, Zr, and Hf) or V (i.e., Nb and Ta) transition metals are substituted into zeolite *BEA, the metals that form stronger Lewis acids give greater selectivities and rates for the desired epoxidation pathway and present smaller enthalpic barriers for both epoxidation and H_2O_2 decomposition reactions. In situ UV−vis spectroscopy shows that these group IV and V materials activate H_2O_2 to form pools of hydroperoxide, peroxide, and superoxide intermediates. Time-resolved UV−vis measurements and the isomeric distributions of Z-stilbene epoxidation products demonstrate that the active species for epoxidations on group IV and V transition metals are only M-OOH/-$(O_2)^{2-}$ and M-$(O_2)^{-}$ species, respectively. Mechanistic interpretations of kinetic data suggest that these group IV and V materials catalyze cyclohexene epoxidation and H_2O_2 decomposition through largely identical Eley−Rideal mechanisms that involve the irreversible activation of coordinated H_2O_2 followed by reaction with an olefin or H_2O_2. Epoxidation rates and selectivities vary over five- and two-orders of magnitude, respectively, among these catalysts and depend exponentially on the energy for ligand-to-metal charge transfer (LMCT) and the functional Lewis acid strength of the metal centers. Together, these observations show that more electrophilic active-oxygen species (i.e., lower-energy LMCT) are more reactive and selective for epoxidations of electron-rich olefins and explain why Ti-based catalysts have been identified as the most active among early transition metals for these reactions. Further, H_2O_2 decomposition (the undesirable reaction pathway) possesses a weaker dependence on Lewis acidity than epoxidation, which suggests that the design of catalysts with increased Lewis acid strength will simultaneously increase the reactivity and selectivity of olefin epoxidation.

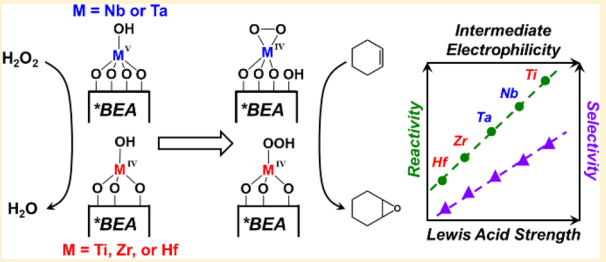

1. INTRODUCTION

Small-molecule oxidations are among the most important and well-studied reactions in synthetic chemistry.[1] Olefin epoxidation is of particular importance, as epoxides (e.g., propylene oxide, styrene oxide, etc.) are important precursors and monomers for the production of pharmaceuticals and epoxy resins.[2−4] Despite the importance of epoxides, current production methods typically involve the use of hazardous organic-peroxide oxidants[4] or caustic waste-producing Cl-containing processes (e.g., the chlorohydrin process).[5] Molecular oxygen (O_2) is utilized for the epoxidation of ethylene (C_2H_4) to form ethylene oxide (EO) over promoted Ag catalysts.[6−9] However, selectivities for C_2H_4 epoxidation with O_2 reach 90%, and 5−10% of C_2H_4 is overoxidized to form massive amounts of CO_2 annually (1.5−3 Mton yr^{-1}),[6] which contributes to global climate change.[10] Furthermore, supported Ag catalysts tend to oxidize allylic positions within hydrocarbons, which prevents the use of these catalysts and O_2 for the epoxidation of molecules larger than C_2H_4.[6]

Hydrogen peroxide (H_2O_2) is a green oxidant that can selectively epoxidize olefins and may replace more environmentally impactful oxidants. Currently, one of the few industrial processes that utilizes H_2O_2 for olefin epoxidation is the hydrogen peroxide−propylene oxide process,[4,11] which couples the anthraquinone auto-oxidation process with a propylene epoxidation facility that catalyzes propylene epoxidations with a microporous titanium silicate zeolite catalyst (TS-1).[12,13] TS-1 gives acceptable H_2O_2 selectivities (80−95%) for propylene epoxidation;[14] however, it is not obvious how other early transition metal-substituted zeolites may perform in epoxidations. Additionally, the differences in epoxidation rates and selectivities between Ti and other early transition metal atoms in zeolite frameworks are not experimentally demonstrated in the open literature and neither are the reasons for such potential differences. Consequently, there are few proven

Received: February 10, 2017
Published: April 28, 2017

DOI: 10.1021/jacs.7b01422
J. Am. Chem. Soc. XXXX, XXX, XXX−XXX

guiding principles for the synthesis of improved microporous catalysts for epoxidations.

Group IV and V metals grafted onto SiO_2 or incorporated into tetrahedral sites within zeolite frameworks effectively activate H_2O_2 and epoxidize olefins.[4,15−23] Monomeric Nb atoms in the *BEA zeolite framework (Nb-β) irreversibly activate H_2O_2 to form superoxide intermediates (i.e., Nb-$(O_2)^-$) that selectively epoxidize olefins.[15] Alternatively, Ti atoms within TS-1 activate H_2O_2 to form Ti-OOH species, which are thought to be active for olefin epoxidation.[24−26] Several computational studies have probed the effects of transition metal atom substitution into zeolite frameworks on the Lewis and Brønsted acid strengths and correlated these changes to predicted reactivity predominantly for biomass conversion or the isomerization of glucose.[27−30] Most relevant to this work, Boronat et al. used quantum chemical calculations to relate the LUMO energy of the transition metal atoms Ti, Zr, and Sn within the framework of zeolite *BEA to the measured rates of octene epoxidation and attributed the relatively high reactivity of Ti-β to a LUMO energy that is lower than those of Zr- and Sn-β.[31] Experimentally, Notestein and co-workers found that the initial rates of cyclohexene epoxidation over group IV and V metals grafted onto silica correlate with the Pauling electronegativity of these metals.[23] In summary, the Lewis acidity of these heterogeneous atomically isolated catalysts has been hypothesized to determine the ability of such species to activate H_2O_2 and the manner by which the activated complex reacts with an olefin.[22,31−36] Interestingly, these trends disagree with a significant body of work on group VII and VIII (e.g., Mn and Fe) homogeneous complexes (e.g., porphyrin- and Schiff-base complexes), for which greater electron densities on the metal centers increase oxidation rates by facilitating the formation of M═O species via heterolytic cleavage of the O−O bond of H_2O_2.[4,37] Connections between the Lewis acid strength of metal-substituted zeolites and epoxidation rates and selectivities have been hypothesized to exist for nearly two decades.[23,31,35,36] However, to the best of our knowledge, no investigations have correlated barriers for epoxidation and H_2O_2 decomposition (i.e., to infer selectivity) to *experimentally* determined descriptors of the strength of the Lewis acid sites or to the electronic structure of the reactive surface intermediates for epoxidation. Furthermore, no studies have compared the identities and relative reactivities of the active hydroperoxo and superoxo intermediates for epoxidation or the ways in which their electronic structures reflect the chemical properties of the transition metal heteroatom on these group IV and V metal-substituted zeolite catalysts.

Here, we incorporate group IV (i.e., Ti, Zr, and Hf) and V (i.e., Nb, and Ta) metal atoms into the framework of zeolite *BEA (M-β) and use reaction rates measured as a function of the reactant concentrations to show that these M-β catalysts catalyze H_2O_2 decomposition and cyclohexene (C_6H_{10}) epoxidation through an identical mechanism that varies only in the structure of the active oxidant. H_2O_2 activates irreversibly to form dioxygen intermediates (M-(O_2)), such as M-$(O_2)^-$ or M-OOH/-$(O_2)^{2-}$, which subsequently react with C_6H_{10} through an Eley−Rideal mechanism to form cyclohexene oxide ($C_6H_{10}O$) or with H_2O_2 to decompose. In situ UV−vis measurements and the distributions of isomeric products from *Z*-stilbene epoxidation demonstrate that only M-$(O_2)^-$ species participate directly in epoxidation on group V Lewis acid sites, whereas only M-OOH/-$(O_2)^{2-}$ intermediates react to form epoxides on group IV Lewis acid sites. Reaction rates and selectivities depend exponentially on the extent of electron exchange between these active intermediates and the metal centers, as shown by the energy of the ligand-to-metal charge transfer (LMCT) bands. The differences between the thermodynamic strengths of the Lewis acidic metal centers were quantified from adsorption isobars for deuterated acetonitrile and compared to activation enthalpies ($\Delta H^{\ddagger}$) for both pathways. These comparisons show that stronger Lewis acids possess both lower $\Delta H^{\ddagger}$ (i.e., increased reactivity) and higher selectivities for the epoxidation of C_6H_{10} by M-(O_2) intermediates. Collectively, these results demonstrate that the rates for catalytic epoxidation on these M-β materials (and likely that in other zeolite frameworks) directly reflect the strength of the Lewis acid site and elucidate the reasons for observed selectivity trends on similar group IV and V heterogeneous catalysts.

2. EXPERIMENTAL METHODS

2.1. Catalyst Synthesis. Group IV and V transition metal atoms were incorporated into tetrahedral positions of the *BEA framework by either solid-state[38] (Zr and Hf) or liquid-phase[15,39,40] (Nb, Ta, and Ti) metal-atom incorporation of dealuminated *BEA following previously published procedures. In short, commercial *BEA (Zeolyst, Si:Al ∼ 12.5, NH_4^+ cation) was contacted with concentrated HNO_3 (Macron Chemicals, 69−70 wt %, 20 cm^3 HNO_3 $g_{zeolite}^{-1}$) at reflux (448 K) for 20 h with the intent to remove Al atoms from the framework to produce solvated $Al(NO_3)_3$. Afterward, the solids were recovered by filtration and washed first with concentrated HNO_3 and then with deionized H_2O (17.8 MΩ). The recovered solids were then heated to 823 at 5 K min^{-1} under flowing dry air (100 cm^3 min^{-1}, Airgas, Ultrazero grade) with the intent to remove residual volatiles and any organic species and to produce Si-β (Si:Al > 1200, determined by ICP-OES).

Ti atoms were incorporated into the framework by liquid-phase incorporation (LPI),[15,39,40] which involved stirring Si-β in dichloromethane (DCM, Fisher Chemicals, Certified ACS Stabilized, 15 cm^3 DCM $g_{zeolite}^{-1}$) under an argon atmosphere using standard Schlenk technique. An appropriate amount of $TiCl_4$ (Sigma-Aldrich, 99.9%) was added dropwise to the stirring suspension of Si-β in DCM and brought to reflux (323 K) for 3 h. Notably, $TiCl_4$ will violently react with moisture in air to release HCl and should be handled carefully in an inert atmosphere. After ∼30 min at reflux, the color of the suspension turned from bleached white to tan.

Nb and Ta atoms were also incorporated into the framework by LPI,[15,39,40] which involved stirring Si-β in isopropanol (IPA, Fisher Chemicals, 15 cm^3 IPA $g_{zeolite}^{-1}$) under an ambient atmosphere. An appropriate amount of $NbCl_5$ (Sigma-Aldrich, 99.9%) or $TaCl_5$ (Sigma-Aldrich, 99%) dissolved in IPA was added to the stirring suspension of Si-β in IPA and heated to 333 K for 3 h. Notably, $NbCl_5$ dissolved in IPA is bright yellow and maintains this color for a short time (∼10 min) upon addition of Si-β, after which the color of the suspension turns white.

For Ti, Nb, and Ta samples, the solvent (i.e., DCM or IPA) was removed in vacuo (via rotovap), and the recovered solids were heated to 823 K at 5 K min^{-1} for 6 h in flowing dry air (100 cm^3 cm^{-1}, Airgas, Ultrazero grade). The heat-treated solids possessed a bleached white color.

Hf- and Zr-incorporated *BEA materials were synthesized via solid-state ion exchange.[38] In brief, Si-β was intimately ground with an appropriate amount of $Hf(OEt)_4$ (Alfa-Aesar, 99.9%) or $Zr(OEt)_4$ (Alfa-Aesar, 99%) to yield a homogeneous solid mixture. The solids were then heated to 823 K at 2 K min^{-1} for 6 h in flowing air (100 cm^3 min^{-1}, Airgas, Ultrazero grade) with the intent to melt the Zr- and $Hf(OEt)_4$ and provide ample time for these species to diffuse into the SiOH pockets within the Si-β crystals prior to decomposition. This process results in Zr- or Hf-β, the colors of which are bleached white and light gray, respectively. This solid-state synthesis method can

DOI: 10.1021/jacs.7b01422
J. Am. Chem. Soc. XXXX, XXX, XXX−XXX

potentially produce extra-framework species (e.g., oligomeric ZrO_x or HfO_x species); however, characterization results (shown below) suggest the fraction of Zr and Hf atoms that exist outside the framework are insignificant. Furthermore, the kinetic analysis (section 3.2 and section S2) and correlations reported here rely only on how rates change with a function of reactant concentration and temperature, such that an error in the site count would be systematically applied and would not alter any conclusions.

2.2. Catalyst Characterization. The transition metal content of each M-β content was determined by inductively coupled plasma-optical emission spectroscopy (ICP-OES, PerkinElmer 2000DV), which was calibrated against known dilution standards. For M_x-β, the subscript refers to the number of metal atoms per unit cell of the *BEA framework quantified by ICP-OES. For all kinetic and in situ spectroscopic measurements (sections 2.3 and 2.4), samples of M-β were prepared to result in 0.6−1 (M atoms) (unit cell)$^{-1}$ (i.e., Si/M ratios > 60). Consequently, statistical arguments show that the M atoms are well-separated from one another and that catalysts will contain only a very small fraction of M-O-M linkages, which is supported also by other characterization methods described below. Furthermore, the postsynthetic modification of Al-β only replaced approximately 1 in 5 Al atoms, which leaves ∼4 silanol nests (unit cell)$^{-1}$. This suggests that all M-β used in this study are highly hydrophilic rather than hydrophobic (as is the case in defectless M-β materials).[41]

Catalyst crystallinity was confirmed by powder X-ray diffraction (p-XRD). X-ray diffractograms were obtained on a Siemens/Bruker D5000 diffractometer with Cu Kα radiation (0.15418 nm) using a step size of 0.02°, taken at 1° min^{-1}, under ambient conditions. The similarities between the X-ray diffractograms (Figure S1) show that the *BEA framework remains intact after dealumination and metal incorporation for all M-β samples.

Band edges (E_g) were determined by analysis of diffuse reflectance UV−vis spectra of the bare M-β materials (Figure S2). Total reflectance spectra were measured at ambient conditions with a UV−vis−NIR spectrophotometer (Agilent CARY 5) equipped with a diffuse reflectance accessory (Harrick cricket). Magnesium oxide (MgO, Sigma-Aldrich, 99.995% trace metals basis) was used as a background for all spectra obtained. Samples were prepared by intimately combining M-β (∼10 mg) with MgO (∼100 mg) using a pestle and mortar. Values of E_g were determined from the x-intercept of the linear portion of the corresponding Tauc plots for each material (Figure S2b).[42] The relatively large value of the band edges (Table 1)

Table 1. Heats of Adsorption for CD_3CN Coordinated to Lewis Acidic Framework Metal Atoms and Band Edge Energies (Measured via DR UV−Vis) for $Nb_{0.6}$-, $Ta_{0.6}$-, $Ti_{1.0}$-, $Zr_{1.0}$-, and $Hf_{1.0}$-β

sample	ΔH_{CD_3CN} (kJ mol^{-1})	band edge (eV)
$Nb_{0.6}$-β	−22 ± 2	4.2
$Ta_{0.6}$-β	−17 ± 1	4.8
$Ti_{1.0}$-β	−31 ± 2	4.0
$Zr_{1.0}$-β	−14 ± 1	5.6
$Hf_{1.0}$-β	−13 ± 1	5.7

for all of the materials (and absence of shoulders toward lower energies) further suggests that transition metal atoms within each of these materials are highly disperse and contain little to no oligomeric or bulk metal-oxide phases.[17]

The incorporation of the transition metal atoms into the *BEA framework was confirmed by vibrational spectra of each sample obtained by attenuated total reflectance IR (ATR-IR) spectroscopy. Samples (∼10 mg) were pressed onto the diamond internal reflection element of an ATR-IR instrument (Bruker Alpha), and spectra were recorded at ambient conditions (Figure S3, 32 scans, 2 cm^{-1} resolution). Figure S3a shows the normalized IR spectra for all M-β, all of which possess nearly identical spectra within the framework stretching region. Figure S3b shows the difference spectra for group IV and V catalysts with respect to that of Si-β, and are all normalized to the well-documented ν(Si-O-M)[15,43] feature at 960 cm^{-1} for clarity. The appearance of this feature at ∼960 cm^{-1} (ν(Si−O-M)) on all M-β shows that the transition metal atoms are incorporated into the *BEA framework upon postsynthetic modification.

The presence of Lewis acid sites was characterized by the IR spectra of adsorbed deuterated acetonitrile (CD_3CN, Cambridge Isotope Laboratories, 99.8% D atom)[44,45] coordinated to M-β using a custom-made transmission cell coupled to an FTIR spectrometer (Bruker, Tensor 37) equipped with a liquid N_2-cooled HgCdTe detector.[46] Catalysts were pressed into self-supporting wafers (∼60 mg) and placed within the stainless-steel cell, which was equipped with CaF_2 windows and connected to a gas manifold by gas-transfer lines that were heated to 423 K via electrical heating tape (Omega, FGH Series). Catalysts were first heated to 423 K (10 K min^{-1}) and held for 1.5 h under flowing He (50 cm^3 min^{-1}, Airgas Ultra High Purity) with the intent to remove any residual H_2O and other volatiles that may have adsorbed during catalyst storage. CD_3CN was fed via a syringe pump (KD Scientific, Legato 100) at 1 μL min^{-1} and vaporized inside the heated gas-transfer lines into a stream of flowing He (50 cm^3 min^{-1}, Airgas, 99.999%) to produce a stream containing 1.0 kPa CD_3CN. IR spectra (Figure S4) of adsorbed CD_3CN were obtained by flowing the CD_3CN/He stream over the sample for 15 min. The flow of CD_3CN was then stopped, and the sample was heated at 10 K min^{-1} to a final temperature of 423 K while FTIR spectra (128 scans, 1 cm^{-1} resolution) were continuously recorded.

Figure 1 shows FTIR spectra for adsorbed CD_3CN on all M-β during the desorption of CD_3CN in flowing He (50 cm^3 min^{-1}, ∼333 K) after saturation of CD_3CN to visualize relevant CD_3CN IR features. All M-β possess an absorbance feature at ∼2274 cm^{-1}, which corresponds to ν(C≡N) of CD_3CN coordinated to SiOH functionalities within the *BEA framework. Ti-, Nb-, and Ta-β each

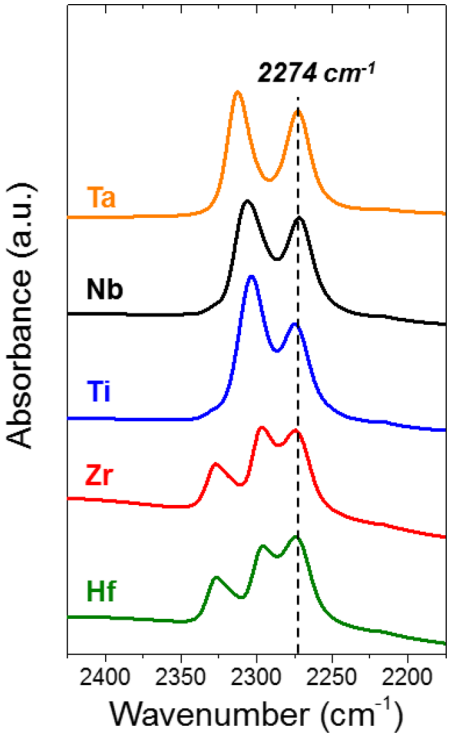

Figure 1. Infrared spectra of CD_3CN bound to Lewis acid, Brønsted acid, and silanol sites on M-β catalysts including $Ti_{1.0}$-β (blue), $Zr_{1.0}$-β (red), $Hf_{1.0}$-β (green), $Nb_{0.6}$-β (black), and $Ta_{0.6}$-β (orange). Spectra are normalized to ν(C≡N) of silanol-bound CD_3CN (2274 cm^{-1}) and were acquired in flowing He (50 cm^3 min^{-1}, ∼373 K) to monitor the desorption of CD_3CN after saturation.

DOI: 10.1021/jacs.7b01422
J. Am. Chem. Soc. XXXX, XXX, XXX−XXX

possess a single additional feature at 2302, 2306, and 2312 cm^{-1}, respectively, which is assigned to $\nu(C{\equiv}N)$ of Lewis acid-bound CD_3CN.[41] Both Zr- and Hf-β possess two additional features at 2326 and 2296 cm^{-1}. Of these two features, the peaks at 2296 cm^{-1} are assigned to CD_3CN coordinated to the Lewis acidic Zr and Hf atoms in the *BEA framework based on recent reports for Zr-β.[47] Finally, CD_3CN bound to Brønsted acid sites on H-exchanged USY[48] has been observed at 2332 cm^{-1}; therefore, the features at 2326 cm^{-1} on Zr- and Hf-β may be attributed to CD_3CN coordinated to Brønsted acid sites (e.g., $(SiO)_3Zr(OH)$), as Zr-β is known to contain Brønsted acid sites at open Zr sites in the framework.[49] Notably, the features at 2326 and 2296 cm^{-1} in Zr- and Hf-β do not correspond to remaining Lewis or Brønsted acidic Al atoms in the framework[41] as these features are not observed in Si-β (Figure S4), nor are they attributed to bulk or oligomeric extra-framework metal oxide clusters.[45]

The presence and ratio of open versus closed sites has been shown to influence the reactivity of similar M-β catalysts. For example, the rates for the conversion of ethanol to butadiene on Zr-β has been shown to be proportional to the number of open Zr sites on a series of materials (as detected by FTIR of adsorbed CO at 100 K),[50] which suggests that butadiene forms primarily on open sites. Gounder and co-workers have used the FTIR spectra of adsorbed CD_3CN to show that Sn-β made by both postsynthetic modification and hydrothermal syntheses contain significant amounts of both open and closed sites, which suggests that it is extremely difficult to synthesize materials that contain solely one type of site.[41] Thus, the M-β materials in this study likely contain a mixture of open and closed sites. However, the relationships developed within this work seek to correlate the experimentally observed reactivity (e.g., quantified by values of $\Delta H^{\ddagger}$, which do not depend on the number of sites) of these materials with a functional descriptor of the Lewis acid strength rather than compare within each material the reactivity of open versus closed sites. Future studies will explore how changes in the prevalence of open or closed sites (e.g., manipulated using hydrothermal synthesis versus postsynthetic modification methods) affect the Lewis acid strength, reactivity, and selectivity of a given group IV or V metal in the framework of these zeolitic materials

To obtain differences between the functional Lewis acid strengths of the catalysts, the enthalpies for adsorption of CD_3CN to Lewis acid sites (ΔH_{CD_3CN}) were determined by monitoring the absorbance value of the $\nu(C{\equiv}N)$ feature as a function of inverse temperature (at a constant partial pressure of CD_3CN (Figure S5, ~1.2 kPa CD_3CN, 373−423 K). The coverage of Lewis acid-bound CD_3CN is proportional to the intensity of the $\nu(C{\equiv}N)$ feature in the absorbance spectra, and the heat of adsorption for CD_3CN onto Lewis acid sites on each of the M-β materials is calculated by the method of van't Hoff (Figure S5). Table 1 summarizes the experimentally determined values of ΔH_{CD_3CN} for all M-β catalysts.

Overall, the results from p-XRD, diffuse reflectance UV−vis spectroscopy, ATR-IR spectra of M-β, and FTIR of adsorbed CD_3CN show that the *BEA framework is intact after postsynthetic modification, very little if any oligomeric or bulk metal oxide is present, metal atoms are incorporated into the framework and the Lewis acid strength is quantified, respectively (section S1; Table 1; Figure 1 and Figures S1−S5).

2.3. Measurements of Reaction Rates and Selectivities. Rates for cyclohexene (C_6H_{10}) epoxidation and H_2O_2 decomposition were measured within batch reactors (100 cm^3, three-neck round-bottom flask) equipped with reflux condensers to minimize evaporative losses. Appropriate amounts of C_6H_{10} (Sigma-Aldrich, 99%) or *cis*-stilbene (Sigma-Aldrich, > 96%) and H_2O_2 (Fischer Chemicals, 30 wt % in H_2O) were added to a solution of acetonitrile (CH_3CN, Macron Chemicals, >99.8%) and benzene (for use as an internal standard, Sigma-Aldrich, thiophene free, >99%) and heated to the desired temperature (303−348 K) while stirring at 600 rpm. Epoxidation and H_2O_2 decomposition was initiated by adding the M-β catalyst. Small aliquots (~300 μL) of the reaction solution were extracted as a function of time through a 0.22 μm syringe filter (with the intent to remove suspended catalyst and quench epoxidation and H_2O_2 decomposition). The hydrocarbon and oxygenate concentrations within these aliquots were quantified via a gas chromatograph (HP-5890, Series A) equipped with a flame-ionization detector. All species were identified and calibration factors were quantified using standards of known concentration. The H_2O_2 concentration of each aliquot was determined by colorimetric titration using an aqueous solution of $CuSO_4$ (8.3 mM, Fisher Chemicals, >98.6%), neocuproine (12 mM, Sigma-Aldrich, >98%), and ethanol (25% v/v, Decon Laboratories Inc., 100%). The concentration of H_2O_2 was quantified from comparison of the absorbance at 454 nm to calibrated standards measured using a visible-light spectrophotometer (Spectronic, 20 Genesys). Test reactions (0.01 M C_6H_{10}, 1 mM H_2O_2, 313 K) with Si-β reveal that no reaction (i.e., C_6H_{10} epoxidation or H_2O_2 decomposition) occurs in the absence of the metal atoms. In all reported data, the carbon balance closed within 98%, and the standard uncertainty for the measured reaction rates was <7%. Rates for the conversion of C_6H_{10} and H_2O_2 on the five M-β were measured as functions of $[H_2O_2]$, $[C_6H_{10}]$, and $[C_6H_{10}O]$, and all reported results were obtained at differential conversion (i.e., <5% conversion of limiting reagent).

Reported rates were measured in the absence of intrapellet mass-transfer limitations, as shown by satisfying the Madon−Boudart criterion for Ti-β (i.e., the M-β catalyst with the greatest turnover rates) by performing reactions under identical conditions with catalysts containing different metal loadings (section S1.2).[51] Over the metal loadings tested, the epoxidation turnover rates did not depend on the metal content, which demonstrates that concentration gradients do not exist within the reactor or within the M-β particles. Additionally, all catalysts tested are of similar metal loadings (group IV ≈ 1 (M atom) (unit cell)$^{-1}$; group V ≈ 0.6 (M atom) (unit cell)$^{-1}$).

2.4. In Situ UV−Vis Spectroscopy. In situ UV−vis spectroscopy was used to identify the intermediates formed upon H_2O_2 activation and determine which of these species were directly responsible for olefin epoxidation. M-β samples were pressed into 7 mm diameter pellets (~5 mg) and loaded into a custom-built UV−vis liquid flow cell equipped with cartridge heaters for temperature control. UV−vis spectra (100 scans, 600 ms integration time) were collected using a 45° diffuse reflection probe (Avantes, solarization-resistant fibers) connected to a fiber-optic spectrometer (Avantes, AvaFast 2048) with a compact deuterium-halogen light source (Avantes, AvaLight-DHc). Reactant and solvent solutions were introduced via a high-performance liquid chromatography pump (Waters, 515). A CH_3CN solution (0.4 M H_2O, 1 cm^3 min^{-1}) flowed over the samples at 313 K for 1 h, and the corresponding UV−vis spectra for each M-β was used as the background for all measurements. The M-β samples were activated with H_2O_2 by switching the flow to a solution of H_2O_2 in CH_3CN (0.1 M H_2O_2, 0.4 M H_2O, 1 cm^3 min^{-1}) at 313 K until the UV−vis spectra became constant (i.e., implying a constant coverage of surface intermediates). Pure CH_3CN (1 cm^3 min^{-1}) was then flowed over the samples at 313 K for 10 min to remove residual H_2O_2. The reactivity of the surface intermediates was determined by continuously acquiring UV−vis spectra while flowing a solution of C_6H_{10} in CH_3CN (0.1 M C_6H_{10}, 0.4 M H_2O, 1 cm^3 min^{-1}) and by mathematically modeling the rates of peak attenuation (section S2). Notably, separate experiments showed that the UV−vis absorbance features on the H_2O_2-activated M-β did not change or attenuate (for a period of 2 h) under a flowing stream of CH_3CN (0.4 M H_2O, 1 cm^3 min^{-1}) or pure H_2O (1 cm^3 min^{-1}, 17.8 MΩ) at 313 K. Processes for peak smoothing, background subtraction, and peak fitting were performed within OriginPro and are described in section S2.

3. RESULTS AND DISCUSSION

3.1. Identifying Active Oxygen Intermediates for Epoxidations. Metal-bound superoxide (M-$(O_2)^-$),[15,52] peroxide (M-$(O_2)^{2-}$),[16,20,24] and hydroperoxide (M-OOH)[24−26,53−55] intermediates have been proposed as the active intermediates for olefin epoxidation on group IV and V catalysts grafted onto SiO_2 and incorporated into zeolite frameworks. However, published results disagree over the exact

DOI: 10.1021/jacs.7b01422
J. Am. Chem. Soc. XXXX, XXX, XXX−XXX

identity of the reactive intermediate on these solid catalysts. The activation of H_2O_2 on group IV (i.e., Ti, Zr, and Hf) and V (i.e., Nb and Ta) transition metal atoms incorporated into the *BEA framework (M-β) likely forms a pool of superoxide, peroxide, and hydroperoxide intermediates, where these complexes may be characterized by their electronic transitions (e.g., ligand-to-metal charge transfer) via UV−vis spectroscopy.

UV−vis spectra of H_2O_2-activated M-β acquired in situ (Figure 2, 0.1 M H_2O_2, 0.4 M H_2O, in CH_3CN, 1 cm^3 min^{-1}, 313 K) show that all M-β materials possess overlapping absorbance features (Figure S8), whose intensities are proportional to the relative surface coverage of these species. Similar overlapping features exist on TS-1,[24,56,57] Nb-β,[15] and bulk Nb_2O_5,[58] where the lower energy (higher wavelength (λ)) features are known to correspond to M-OOH/M-$(O_2)^{2-}$ species while the higher energy (lower λ) peaks are assigned to the M-$(O_2)^-$ species.[15,24,52,58,59] As such, we systematically assign the higher λ features in Ta-, Zr-, and Hf-β to the M-OOH/-$(O_2)^{2-}$ species and the lower λ feature to M-$(O_2)^-$.

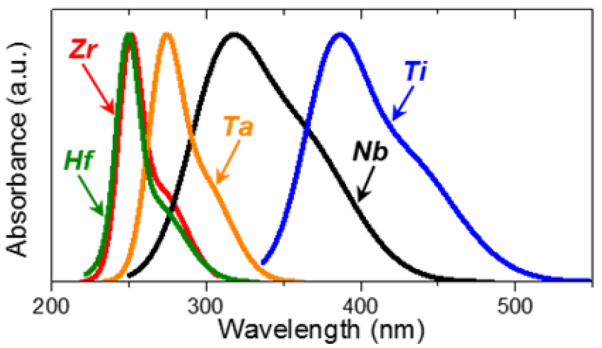

Figure 2. UV−vis spectra of H_2O_2-activated (section 2.4) M-β catalysts including $Hf_{1.0}$-β (green), $Zr_{1.0}$-β (red), $Ta_{0.6}$-β (orange), $Nb_{0.2}$-β (black), and $Ti_{1.0}$-β (blue). Spectra were acquired in situ in flowing H_2O_2 in CH_3CN (0.1 M H_2O_2, 0.4 M H_2O, 1 cm^3 min^{-1}) at 313 K. $Nb_{0.2}$-β data is adapted from ref 15.

Scheme 1 shows the possible reaction of both the M-OOH/-$(O_2)^{2-}$ and M-$(O_2)^-$ intermediates with C_6H_{10}, where the differences in the rates of consumption of these species in the presence of C_6H_{10} will reflect the relative reactivity of these intermediates. However, to accurately estimate values of rate constants for the reaction of dioxygen species with C_6H_{10} (i.e., k_c and k_d), the analysis must account for the interconversion of these species via reversible isomerization and charge transfer processes (section S2.3 discusses how the interconversion of the two intermediates is accounted for during the transient kinetic analysis).[15,60]

Scheme 1. Interconversion and Consumption of M-OOH/M-$(O_2)^{2-}$ (M-OOH Shown) and M-$(O_2)^-$ Species upon Reaction with C_6H_{10}[a]

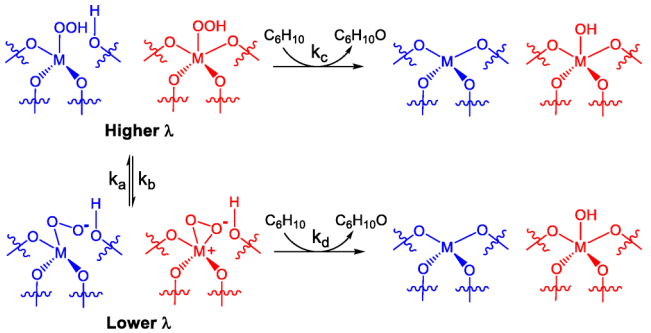

[a]Color coding is for clarity: group IV (Ti, Zr, and Hf = blue) and V (Nb and Ta = red).

The UV−vis absorbance features for species on Ti-, Nb-, and Ta-β attenuate exponentially with time upon exposure to flowing C_6H_{10} (0.1 M C_6H_{10}, 0.4 M H_2O, in CH_3CN, 313 K). Figure 3 shows the change in the normalized surface coverages of these species as a function of time and indicates clearly that specific intermediates are more reactive than others on a given M-β catalyst. Specifically, the number of Ti-OOH/-$(O_2)^{2-}$ species diminish at a faster rate than those for Ti-$(O_2)^-$, whereas the opposite is observed for Nb- and Ta-β. Table 2 shows rate constants for the reaction between M-$(O_2)^-$ or M-OOH/-$(O_2)^{2-}$ intermediates and C_6H_{10} (Scheme 1) on each catalyst that are calculated from the change in the normalized

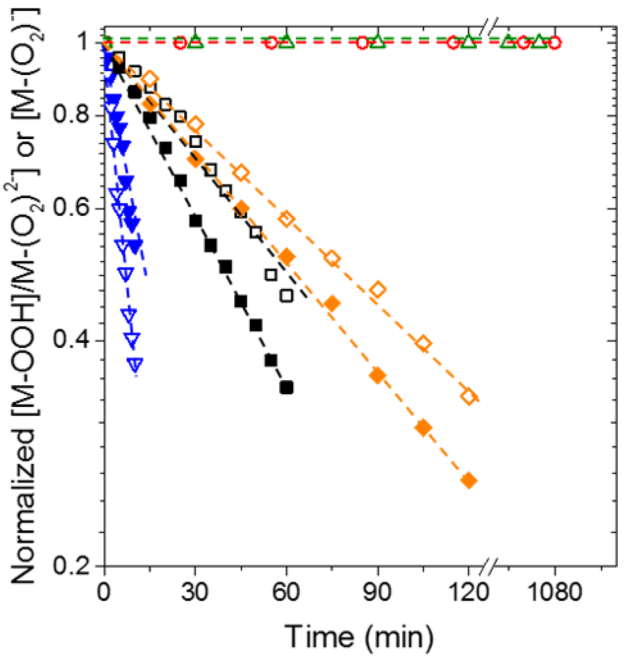

Figure 3. Change in the normalized surface coverage of M-OOH/M-$(O_2)^{2-}$ (open symbols) and M-$(O_2)^-$ (closed symbols) species as a function of time for $Ti_{1.0}$-β (blue ▼), $Zr_{1.0}$-β (red ●), $Hf_{1.0}$-β (green triangle▲), $Nb_{0.2}$-β (■), and $Ta_{0.6}$-β (orange ◆). UV−vis spectra were acquired in situ upon flowing C_6H_{10} in CH_3CN (0.1 M C_6H_{10}, 0.4 M H_2O, 1 cm^3 min^{-1}) over H_2O_2-activated samples (section 2.4) at 313 K. $Nb_{0.2}$-β data is adapted from ref 15. Closed symbols for $Zr_{1.0}$- and $Hf_{1.0}$-β coincide with the open symbols. Note that the *Y*-axis is shown on a logarithmic scale.

Table 2. Evidence for the Direct Involvement of Specific Intermediates in Olefin Epoxidation: Rate Constants for the Epoxidation of C_6H_{10} and *Z:E* (*cis:trans*) Stilbene Oxide Product Ratios from the Epoxidation of *Z*-Stilbene

sample	k_c (s^{-1})	k_d (s^{-1})	*Z:E* ratio
$Ti_{1.0}$-β	2.9×10^{-2}	1.7×10^{-4}	9.2
$Nb_{0.2}$-β	2.2×10^{-7}	4.5×10^{-3}	1.0
$Ta_{0.6}$-β	1.0×10^{-4}	3.3×10^{-3}	1.0
$Zr_{1.0}$-β	$<10^{-6}$	$<10^{-6}$	7.1
$Hf_{1.0}$-β	$<10^{-6}$	$<10^{-6}$	6.3

DOI: 10.1021/jacs.7b01422
J. Am. Chem. Soc. XXXX, XXX, XXX−XXX

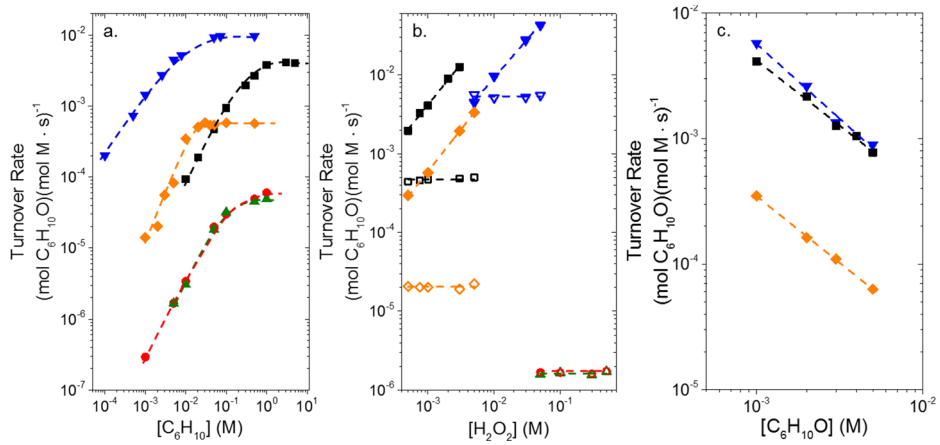

Figure 4. Turnover rates for the formation of $C_6H_{10}O$ as a function of (a) C_6H_{10} over $Nb_{0.6}$-β (■, 1 mM H_2O_2, 313 K), $Ta_{0.6}$-β (orange ◆, 1 mM H_2O_2, 313 K), $Ti_{1.0}$-β (blue ▼, 0.01 M H_2O_2, 313 K), $Zr_{1.0}$-β (red ●, 0.1 M H_2O_2, 323 K), and $Hf_{1.0}$-β (green ▲, 0.1 M H_2O_2, 323 K), (b) H_2O_2 over $Nb_{0.6}$-β (□, 0.05 M C_6H_{10}, ■, 3 M C_6H_{10}, 313 K), $Ta_{0.6}$-β (orange ◇, 2 mM C_6H_{10}, orange ◆, 0.5 M C_6H_{10}, 313 K), $Ti_{1.0}$-β (blue ▽, 0.05 M C_6H_{10}, blue ▼, 0.5 M C_6H_{10}, 313 K), $Zr_{1.0}$-β (red ○, 5 mM C_6H_{10}, 323 K), and $Hf_{1.0}$-β (green △, 5 mM C_6H_{10}, 323 K), and (c) $C_6H_{10}O$ over $Nb_{0.6}$-β (■, 3 M C_6H_{10}, 1 mM H_2O_2, 313 K), $Ta_{0.6}$-β (orange ◆, 0.5 M C_6H_{10}, 1 mM H_2O_2, 313 K), $Ti_{1.0}$-β (blue ▼, 0.5 M C_6H_{10}, 0.01 M H_2O_2, 313 K). Dashed lines are intended to guide the eye. Nb-β data is adapted from ref 15.

intensity of the corresponding spectral features for each species (Figure 3) during the reaction of H_2O_2-activated M-β with flowing C_6H_{10} at conditions similar to those for rate measurements (section S2.3). The calculated rate constants (Table 2 and Table S2) for epoxidation by M-$(O_2)^-$ on Nb- and Ta-β are 2×10^4- and 32-times larger than for epoxidation by M-OOH/-$(O_2)^{2-}$, respectively, which suggests that superoxide species are the active intermediates for epoxidation on group V substituents in the *BEA.[15] However, for Ti-β, the rate constant for the consumption of Ti-OOH/-$(O_2)^{2-}$ (i.e., k_c) is larger than that for Ti-$(O_2)^-$ (i.e., k_d) by a factor of 170. This difference shows that the Ti-OOH/-$(O_2)^{2-}$ species are primarily responsible for olefin epoxidation on Ti-β, which agrees with the intermediates proposed for epoxidation reactions on TS-1.[25,26,57,60,61] The attenuation of the UV−vis absorbance features for Zr- and Hf-β were negligible on the time scale of the experiment, which corresponds to rate constants for epoxidation with these intermediates of $<10^{-6}$ s^{-1} and is consistent with kinetic measurements for these materials (i.e., the rates of reaction for Zr- and Hf-β are a factor of $\sim 10^5$ less than Ti-β at comparable conditions (Figure 5)). The values of k_c and k_d could not be determined on Zr-β and Hf-β because the attenuation rates were immeasurable; however, the identities of the H_2O_2-derived intermediates responsible for epoxidation on these materials were determined using an alternative method that is described next.

Epoxidation reactions with *Z*-stilbene were used to support the identifications of the active intermediates derived from the in situ UV−vis measurements. Olefin epoxidations that involve M-OOH/-$(O_2)^{2-}$ species occur through a concerted mechanism, where oxygen-atom transfer from the active intermediate to the olefin occurs in a single step and thus prevents stereochemical rearrangement (e.g., C−C bond rotation).[4,26,62] Such epoxidations result in the nearly exclusive formation of *Z*-stilbene oxide. Epoxidations that use M-$(O_2)^-$ intermediates, however, react through a biradical mechanism that allows nearly unhindered rotation about the C═C bond and therefore gives distributions of epoxide products that contain comparable amounts of *E*- and *Z*-stilbene oxide isomers.[15,63,64] Table 2 shows that group IV (i.e., Ti, Zr, and Hf) catalysts preferentially form *Z*-stilbene oxide, whereas group V (i.e., Nb and Ta) produce nearly equal amounts of *Z*- and *E*-stilbene oxide. The microporous nature of these materials does not introduce artifacts in the analysis or the interpretation of these isomer distributions. The disparity in the *Z*:*E* ratio of stilbene oxide between group IV and V metals (Table 2), suggests that the pore geometry has minimal, if any, effect on the distribution of products. An in situ UV−vis experiment was performed on H_2O_2-activated Ti-β (Figure S9) to determine if *Z*-stilbene was able to diffuse into the *BEA framework and react with all Ti-atoms within the bulk. The absorbance features for both M-OOH/-$(O_2)^{2-}$ and M-$(O_2)^-$ attenuated exponentially and indicate that ~95% of the intermediates were consumed, which strongly suggests that the *Z*-stilbene is able to fully access the pores of M-β and react. Consequently, the *E*- and *Z*-stilbene oxide isomers form by reactions that occur on the same sites and with the same intermediates that facilitate C_6H_{10} epoxidation and not on a subset of sites on the exterior surface of the catalyst particles. These product isomer distributions, in conjunction with in situ UV−vis measurements (Figure 3) and the calculated rate constants (Table 2), strongly suggest that the reactive intermediate(s) responsible for olefin epoxidation on group IV (i.e., Ti, Zr, and Hf) catalysts are the M-OOH/-$(O_2)^{2-}$ species, whereas group V (i.e., Nb and Ta) materials react through an M-$(O_2)^-$ intermediate.

3.2. Mechanistic Interpretation of Kinetic Data. Figure 4a shows turnover rates for the formation of cyclohexene oxide ($C_6H_{10}O$) as a function of $[C_6H_{10}]$ (10^{-4}−5 M) at constant $[H_2O_2]$ over all M-β; Figure 4b shows turnover rates for $C_6H_{10}O$ formation as a function of $[H_2O_2]$ at constant $[C_6H_{10}]$, and Figure 4c shows $C_6H_{10}O$ formation rates as a function of $[C_6H_{10}O]$ at constant $[H_2O_2]$ and $[C_6H_{10}]$. In all cases, rates of epoxidation depend linearly on $[C_6H_{10}]$ (Figure 4a) and do not depend on $[H_2O_2]$ (Figure 4b) at relatively low $[C_6H_{10}]$:$[H_2O_2]$, which suggests that the active sites are saturated with a H_2O_2-derived intermediate at these conditions. As $[C_6H_{10}]$:$[H_2O_2]$ reactant ratios increase, the rate of epoxidation eventually becomes independent of $[C_6H_{10}]$ (Figure 4a), proportional to $[H_2O_2]$ (Figure 4b, Ti-, Nb-, and Ta-β), and inversely proportional to $[C_6H_{10}O]$ (Figure 4c). This change suggests that the identity of the most abundant surface intermediate (MASI) changes to a C_6H_{10}-derived

DOI: 10.1021/jacs.7b01422
J. Am. Chem. Soc. XXXX, XXX, XXX−XXX

Scheme 2. Proposed Mechanism for the Epoxidation of C_6H_{10} with H_2O_2 over Group IV (Ti, Zr, and Hf, M-OOH Shown, Blue) and Group V (Nb and Ta, Red) M-β. The ⇄ Symbol with 0 Represents a Quasi-Equilibrated Step and the ⇄ Symbol with ∧ Represents a Kinetically Relevant Step[a]

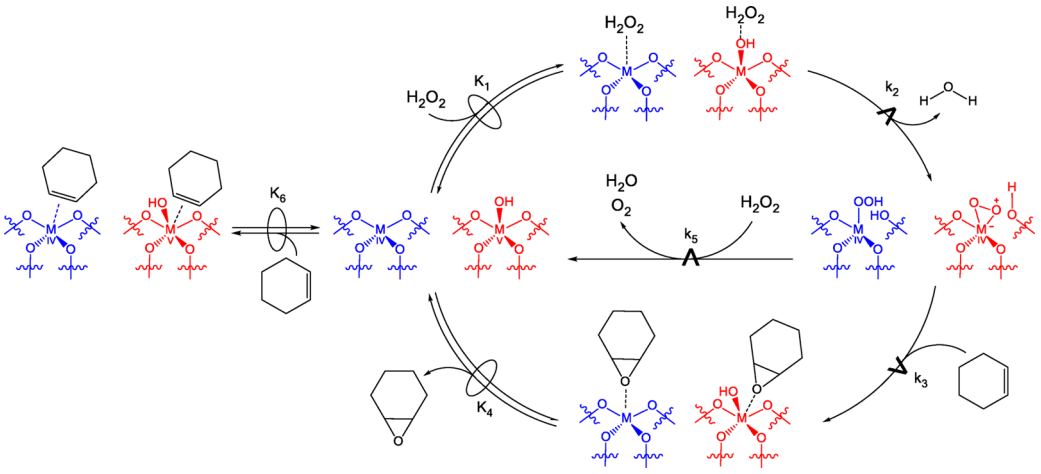

[a]The unoccupied metal atoms are meant to be representations of an empty site rather than suggest all metal atoms exist as closed sites, as both open and closed sites likely exist in these materials (see characterization results in section 2.2).

intermediate (e.g., most likely $C_6H_{10}O$). Conceptually, this occurs because C_6H_{10} and its derivatives displace H_2O_2-derived species from the metal centers at high values of $[C_6H_{10}]$. Notably, the effect of $[C_6H_{10}O]$ on epoxidation turnover rates on Zr- and Hf-β (comparable to Figure 4c) could not be measured because catalytic turnover rates at high $[C_6H_{10}]$ (>1 M) were obscured by noncatalytic C_6H_{10} oxidation rates (i.e., homogeneous reactions).

Scheme 2 shows a series of elementary steps that account for the measured effects of $[C_6H_{10}]$ (Figure 4a), $[H_2O_2]$ (Figure 4b), and $[C_6H_{10}O]$ (Figure 4c) on both rates of C_6H_{10} epoxidation and of H_2O_2 decomposition (H_2O_2 decomposition rate expression is derived in section S3.2).[15] The catalytic cycle for epoxidation involves the quasi-equilibrated adsorption of H_2O_2 (step 1),[15,16,51] followed by the irreversible activation of H_2O_2 (step 2) to form a pool of M-$(O_2)^-$ and M-OOH/-$(O_2)^{2-}$ active intermediates (referred to collectively as M-(O_2)).[4,15,25,60,65] Among these species, either M-OOH/-$(O_2)^{2-}$ or M-$(O_2)^-$ then reacts with C_6H_{10} (depending on the metal identity, section S3.1) via an Eley−Rideal mechanism to form $C_6H_{10}O$ (step 3), which desorbs (step 4). The M-(O_2) species may also decompose nonproductively by reaction with H_2O_2 (step 5). Measured C_6H_{10} epoxidation rates represent the kinetically relevant reaction of the active form of the oxidizing surface intermediate with a C_6H_{10} molecule

$$r_E = k_3[\text{M-O}_2][C_6H_{10}] \tag{1}$$

where r_E is the rate of C_6H_{10} epoxidation, [M-(O_2)] is the number of the M-OOH/-$(O_2)^{2-}$ (group IV) or M-$(O_2)^-$ (group V) species, and k_x is the rate constant for step x in Scheme 2. Application of the pseudosteady state hypothesis to the M-(O_2) intermediates, in combination with a site balance to account for all surface species (full derivation in section S3.1) provides

$$\frac{r_E}{[L]} = \frac{\frac{k_2k_3K_1[C_6H_{10}][H_2O_2]}{(k_3[C_6H_{10}] + k_5[H_2O_2])}}{\beta} \tag{2}$$

where [L] is the total number of M atoms (i.e., active sites) present during the reaction, and β describes the sum of terms representing all potential surface intermediates

$$\beta = 1 + K_6[C_6H_{10}] + K_1[H_2O_2] + \frac{k_2K_1[H_2O_2]}{(k_3[C_6H_{10}] + k_5[H_2O_2])} + K_4[C_6H_{10}O] \tag{3}$$

where K_x is the equilibrium constant for each step x, such that the five terms in β correspond to the number of sites occupied by CH_3CN (i.e., the solvent), C_6H_{10}, H_2O_2, -(O_2) species, and $C_6H_{10}O$, respectively. At high $[H_2O_2]$:$[C_6H_{10}]$ reactant ratios (e.g., 10 for Ti-β), M-(O_2) species become MASI, which is shown by epoxidation rates that increase linearly with $[C_6H_{10}]$ and do not depend on $[H_2O_2]$ (Figure 4). In this limit, eq 2 simplifies to the form

$$\frac{r_E}{[L]} = k_3[C_6H_{10}] \tag{4}$$

which is consistent with the measured dependence of r_E on the reactant concentrations (Figure 4). Similarly, at lower ratios of $[H_2O_2]$:$[C_6H_{10}]$, the reaction product ($C_6H_{10}O$) becomes the MASI as indicated by epoxidation rates that are independent of $[C_6H_{10}]$ and proportional to $[H_2O_2]$ (Figure 4b) but also inversely dependent on $[C_6H_{10}O]$ (Figure 4c, observed on Ti-, Nb-, and Ta-β). When $C_6H_{10}O$ is the MASI, the rate of epoxidation is much greater than the rate of H_2O_2 decomposition (i.e., $k_3[C_6H_{10}] \gg k_5[H_2O_2]$; section S3.2), and eq 2 simplifies to yield

$$\frac{r_E}{[L]} = \frac{k_2K_1[H_2O_2]}{k_5K_4[C_6H_{10}O]} \tag{5}$$

Notably, the form of eq 5 matches the ways in which r_E changes with variations in $[C_6H_{10}]$ and $[H_2O_2]$ as well as $[C_6H_{10}O]$.

Figure 5 shows that these M-β catalysts all have very different turnover rates and selectivities (i.e., productive use of H_2O_2) at standardized conditions (5 mM C_6H_{10}, 5 mM H_2O_2, 313 K). For example, Ti-β gives turnover rates that are a factor of 10^5 (i.e., 100,000)-times greater and selectivities that are 60-times

DOI: 10.1021/jacs.7b01422
J. Am. Chem. Soc. XXXX, XXX, XXX−XXX

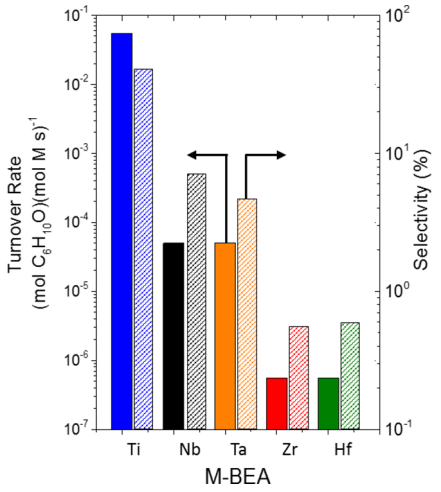

Figure 5. Turnover rates for the formation of $C_6H_{10}O$ (solid) and H_2O_2 selectivities (taken as the ratio of the turnover rate for $C_6H_{10}O$ formation to total H_2O_2 consumption, striped) for $Ti_{1.0}$-β (blue), $Nb_{0.6}$-β (black), $Ta_{0.6}$-β (orange), $Zr_{1.0}$-β (red), and $Hf_{1.0}$-β (green) (5 mM C_6H_{10}, 5 mM H_2O_2, at 313 K).

greater than those on Zr-β (one element down group IV), whereas changing the metal from Nb to Ta results in minimal changes in rates and selectivities. Epoxidation rates depend on $[C_6H_{10}]$, $[H_2O_2]$, and $[C_6H_{10}O]$ in similar ways on all M-β, which strongly suggests that these materials catalyze olefin epoxidation with H_2O_2 through the common mechanism shown in Scheme 2. The reasons for such large differences in turnover rates and selectivities and the disparity between group IV and V catalysts must be related to consequential differences in the electronic structure and reactivity of the involved intermediates. Moreover, these differences must produce activation barriers for epoxidation and H_2O_2 decomposition that depend on both the elemental identity and details of how these transition metal atoms are coordinated within the *BEA framework. Revealing the reasons for these differences requires both quantitative measurements of the activation barriers and methods to probe the chemical properties of the active sites and the electronic structure of the reactive intermediates that bind to these sites. For equitable comparisons to be made among activation barriers for epoxidation and H_2O_2 decomposition reactions, all M-β materials must be evaluated within the same kinetic regime (i.e., at comparable surface coverages, MASI).

Table 3 shows activation enthalpies ($\Delta H^{\ddagger}$) and entropies ($\Delta S^{\ddagger}$) for both C_6H_{10} epoxidation ($\Delta H^{\ddagger}_E$ and $\Delta S^{\ddagger}_E$) and H_2O_2 decomposition ($\Delta H^{\ddagger}_D$ and $\Delta S^{\ddagger}_D$) obtained on M-(O_2) saturated surfaces (i.e., where rates are proportional to $[C_6H_{10}]$ and independent of $[H_2O_2]$ in Figure 4) by operating at high $[H_2O_2]$:$[C_6H_{10}]$ reactant ratios and by measuring rates of reaction as a function of inverse temperature (section S3.3, Figure S11). Notably, values of $\Delta S^{\ddagger}_E$ and $\Delta S^{\ddagger}_D$ do not change systematically with the identity of the metal because these activation entropies largely reflect the loss of translational entropy that results from the coordination of either C_6H_{10} or H_2O_2 to the activated catalyst for epoxidation and H_2O_2 decomposition pathways, respectively. Table 3 shows that values of $\Delta H^{\ddagger}$ are much smaller for Ti-β (the catalyst with the greatest turnover rates), somewhat larger for Nb- and Ta-β, and ~50 kJ mol^{-1} greater on Zr- and Hf-β (the catalysts with the lowest turnover rates). Although these active site structures are similar in coordination (among Ti-, Hf-, and Zr-β), clearly the 10^5-fold difference in rates (Figure 5) and 50 kJ mol^{-1} change in $\Delta H^{\ddagger}_E$ must reflect some intrinsic property of the metal atom, how the metal coordinates to the framework, and properties of the M-(O_2) species (i.e., active intermediate).

Table 3. Activation Enthalpies and Entropies for C_6H_{10} Epoxidation ($\Delta H^{\ddagger}_E$ and $\Delta S^{\ddagger}_E$) and H_2O_2 Decomposition ($\Delta H^{\ddagger}_D$ and $\Delta S^{\ddagger}_D$) over M-β Catalysts and Measured on M-(O_2) Saturated Sites

sample	$\Delta H^{\ddagger}_E$ (kJ mol^{-1})	$\Delta S^{\ddagger}_E$ (J mol^{-1} K^{-1})	$\Delta H^{\ddagger}_D$ (kJ mol^{-1})	$\Delta S^{\ddagger}_D$ (J mol^{-1} K^{-1})
$Nb_{0.6}$-β	72 ± 5	−35 ± 21	45 ± 5	−91 ± 30
$Ta_{0.6}$-β	86 ± 6	−19 ± 11	56 ± 5	−61 ± 25
$Ti_{1.0}$-β	43 ± 5	−53 ± 30	31 ± 10	−104 ± 40
$Zr_{1.0}$-β	91 ± 10	−31 ± 9	65 ± 8	−55 ± 25
$Hf_{1.0}$-β	93 ± 7	−26 ± 8	64 ± 6	−77 ± 21

Previous studies have attempted to relate the reactivity of site-isolated group IV and V metal atoms grafted onto mesoporous SiO_2 to the Pauling electronegativity (E_x, where x represents the elemental identity) of the metal.[23,66,67] Values of $\Delta H^{\ddagger}$ and E_x among the different M-β catalysts appear to correlate linearly for Nb-, Ta-, Zr-, and Hf-β, and $\Delta H^{\ddagger}$ values decrease with increasing electronegativity (Figure S12); however, the values of $\Delta H^{\ddagger}$ for both reactions (i.e., C_6H_{10} epoxidation and H_2O_2 decomposition) on Ti-β are grossly overestimated (by 40 kJ mol^{-1}) by this trend. The fact that E_x values alone are not enough to predict reactivity is not surprising because the electronic structure of the metal sites and their Lewis acid strength should reflect, in part, their coordination environment within the zeolite framework. This same consideration also indicates that the E_x of the metal atoms should not be an accurate predictor for the properties of the active oxidizing intermediates (i.e., M-OOH/-$(O_2)^{2-}$ for group IV or M-$(O_2)^{-}$ for group V). Therefore, a complete understanding of the role that metal identity has for epoxidation with H_2O_2 requires measurements of the functional differences between the Lewis acid strength of the metal centers (as they exist in the zeolite framework) and the electronic structures of the reactive intermediates (acquired in situ).

3.3. Importance of Lewis Acid Strength and Electronic Structure for Olefin Epoxidation. The enthalpy of adsorption of CD_3CN (ΔH_{CD_3CN}) coordinated to Lewis acid sites provides a direct and quantitative measure of the Lewis acid strength for all M-β. Values of ΔH_{CD_3CN} were determined by van't Hoff analysis of CD_3CN adsorption isobars as a function of inverse temperature (Figure S5, Table 1). These measurements were acquired using transmission infrared (IR) spectroscopy to quantify the change in the coverage of CD_3CN at individual Lewis acid sites (section 2.2) by monitoring the intensity of the specific ν(C≡N) feature of interest within the range of 2295−2320 cm^{-1}. This approach distinguishes between the amounts of CD_3CN adsorbed by physisorption to the zeolite framework, coordination to surface silanol groups, and strong chemisorption to Lewis acid sites, because each adsorption mode produces a distinct ν(C≡N) absorbance feature in the IR spectra (Figure S4).[35,44] Consequently, IR spectroscopy allows measurements of ΔH_{CD_3CN} at distinct Lewis acid sites, whereas conventional calorimetric methods would give ensemble averaged values that would lack specificity for CD_3CN molecules adsorbed to Lewis acid sites.

DOI: 10.1021/jacs.7b01422
J. Am. Chem. Soc. XXXX, XXX, XXX−XXX

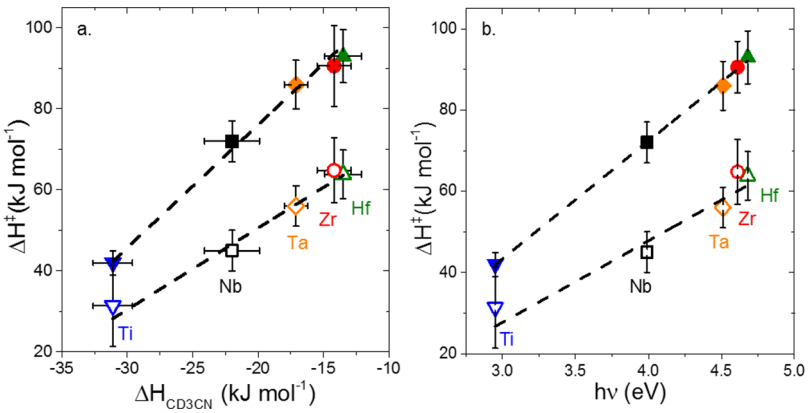

Figure 6. Comparisons between activation enthalpies for C_6H_{10} epoxidation ($\Delta H^{\ddagger}_E$, solid symbols) and H_2O_2 decomposition ($\Delta H^{\ddagger}_D$, open symbols) for M-(O_2)-saturated surfaces of M-β catalysts and measured (a) heats of adsorption for acetonitrile to the active sites ($\Delta H^{\ddagger}_{CD_3CN}$; Table 1) and (b) ligand-to-metal charge transfer (LMCT) energies (Table S1) of the specific reactive intermediate identified on each catalyst for Ti-β (blue ▼), Nb-β (■), Ta-β (orange ◆), Zr-β (red ●), and Hf-β (green ▲). Dashed lines represent linear fits.

Figure 6a shows that values of $\Delta H^{\ddagger}_E$ and $\Delta H^{\ddagger}_D$ depend linearly on ΔH_{CD_3CN} for all M-β catalysts, which strongly suggests that stronger Lewis acids (i.e., more negative ΔH_{CD_3CN}) possess lower activation enthalpies for both C_6H_{10} epoxidation and H_2O_2 decomposition. These trends show that stronger Lewis acid sites give greater turnover rates (Figures 4–6), lower $\Delta H^{\ddagger}$ values (Table 3), and greater selectivities for epoxidation (Figure 5) because strong acids pull electron density away from the -$(O_2)^-$ or -OOH/-$(O_2)^{2-}$ moiety, making these oxidants more electrophilic and reactive. Consequently, these surface species are more reactive toward electron-rich functions of C_6H_{10} (i.e., the C=C) and H_2O_2 (i.e., the lone pairs of O).[68] The phenomena observed here was alluded to by Boronat et al., who predicted that among Lewis acidic metal atoms within the *BEA framework those with a lower-energy LUMO would give greater rates for the epoxidation of olefins.[31] Additionally, these experimentally determined descriptors of the Lewis acid strength (i.e., ΔH_{CD_3CN}) and the electronic structure of the reactive intermediate (i.e., LMCT energy, discussed below (Figure 6b)) also show the reasons for the large differences in selectivity for H_2O_2 use in the epoxidations (discussed next). To the best of our knowledge, these data provide the first clear link between both the turnover rates and selectivities of M-β catalysts for epoxidation that span multiple groups in the periodic table and show how these catalytic properties depend on the Lewis acid strength of the active sites and also the electronic structure of the reactive species that are formed.

Furthermore, the difference in the slopes for $\Delta H^{\ddagger}_E$ (~3) and $\Delta H^{\ddagger}_D$ (~2) as a function of ΔH_{CD_3CN}, show that the most electrophilic M-(O_2) intermediates give the greatest selectivities for epoxidation (Figure 5), which is industrially desirable. Figure 5 shows that H_2O_2 selectivities increase by nearly a factor of 60 under these conditions when the framework metal atom changes from Hf (~0.5%) to Ti (38%). Note that different reaction conditions are used to optimize the H_2O_2 selectivity on the most selective material (e.g., selectivities exceeding 95% for Ti-β at high $[C_6H_{10}]$:$[H_2O_2]$). For all M-β, C_6H_{10} epoxidation (section 3.2) and H_2O_2 decomposition (section S3.2) occur through an Eley–Rideal mechanism between C_6H_{10} or H_2O_2 with the active M-(O_2) intermediate,[15,54] which when combined with the observed dependencies of $\Delta H^{\ddagger}_E$ and $\Delta H^{\ddagger}_D$ on ΔH_{CD_3CN} suggests that there is a stronger interaction of C_6H_{10} with the M-(O_2) species than H_2O_2 in the transition state. This trend differs from a previously proposed O–O bond homolysis mechanism for H_2O_2 decomposition over TS-1,[56,69] where increasing Lewis acid strength was thought to decrease H_2O_2 decomposition rates by pulling electron density from the -(O_2) moiety and thus decreases the propensity for O–O bond cleavage. The data and conclusions here (i.e., Figure 6, more electrophilic intermediates yield greater epoxidation rates) are consistent with the prior observation that epoxidation turnover rates increase with the electron richness of the olefin (e.g., allyl alcohol > allyl chloride > 1-hexene).[4,26] Importantly, here the electronic structure of the active site was modified (and by extension the structure and form of the reactive dioxygen intermediate that is active for epoxidation) by changing the identity of the transition metal substituent, whereas the earlier studies manipulated rates by changing the structure of the reactant.

Figure 6b shows that $\Delta H^{\ddagger}_E$ and $\Delta H^{\ddagger}_D$ also increase linearly with the energy for LMCT (assessed by UV–vis) for the active intermediate (i.e., specifically M-$(O_2)^-$ species for group V and M-OOH/-$(O_2)^{2-}$ for group IV, Figure 2 and Figure S8) on all M-β. Higher LMCT energies reflect weaker Lewis acid sites because these catalysts have a lower tendency to pull electron density toward the metal nuclei. As such, electronic transitions in weaker Lewis acids (e.g., Hf) require higher-energy photons as the electrons have the preference to reside on the -OOH/-$(O_2)^{2-}$ or -$(O_2)^-$ moiety. Conversely, a strong Lewis acid (i.e., Ti) has the tendency to pull electron density to the metal center, resulting in a lower energy LMCT as there is a smaller energetic preference for the electrons to reside on the -OOH/-$(O_2)^{2-}$ or -$(O_2)^-$ moiety. These differences correlate with the $\Delta H^{\ddagger}_E$ and $\Delta H^{\ddagger}_D$ values and show that the M-O_2 species with the greatest degree of electrophilicity are the most reactive and selective for olefin epoxidation.

Table 1 (section 2.2) contains ΔH_{CD_3CN} values for each M-β catalyst and Figure S13 shows that Lewis acid strength (quantified by the value of ΔH_{CD_3CN}) appears to correlate linearly with the values of E_{Nb}, E_{Ta}, E_{Zr}, and E_{Hf}, but E_{Ti} deviates sharply from this trend. Recently, Román et al. measured the chemical shifts of ^{15}N within labeled pyridine coordinated to defectless M-β materials (using MAS NMR) and correlated

DOI: 10.1021/jacs.7b01422
J. Am. Chem. Soc. XXXX, XXX, XXX–XXX

these shifts to the Mulliken electronegativities (χ_x, where x is the metal identity) and calculated (via DFT methods) metal-pyridine bond dissociation energies.[70] Figure S14 shows ΔH_{CD_3CN} plotted as a function of χ_x and suggests that there is no obvious relationship between the measured Lewis acid strength and χ_x. The discrepancies in the relationship between Lewis acidity and Pauling/Mulliken electronegativity likely reflect differences in the coordination environment of the metal center. For example, group V metals (i.e., Nb and Ta) are penta-coordinated in *BEA with typically four -O-Si bonds to the framework and an appendage -OH group (i.e., closed sites),[15,71,72] whereas group IV metals (i.e., Ti, Zr, and Hf) are tetra-coordinated and exist with four framework -O-Si bonds (i.e., closed sites) or three framework bonds and a terminal -OH (i.e., open sites).[19,45,73] Consequently, the reactivity of elements within the same group may correlate with E_x or χ_x; however, more meaningful comparisons that extend across the periodic table and which capture potential variations in the coordination of the metal to the zeolite framework require more direct measurements of the properties of the active sites and active intermediates that exist in the catalyst, such as those presented here.

The structure−function relationships elucidated here (Figure 6) for group IV and V transition metal atoms within a zeolite framework directly oppose the widely accepted electronic relationships described for homogeneous porphyrin and Schiff-base catalysts.[4,37] These homogeneous complexes are generally constructed to result in increased electron density at the metal center (generally Fe or Mn) to facilitate homolysis of the M-OOH species and yield active oxo (M=O) or oxene (M^+=O) intermediates. In contrast, epoxidation rates and selectivities of these group IV and V catalysts increase exponentially with Lewis acid strength, whereas increased electron density (as is beneficial to porphyrin and Schiff-base complexes) on the metal centers would lead to lower epoxidation rates and selectivities.

4. CONCLUSIONS

In situ UV−vis spectroscopy shows that group IV (i.e., Ti, Zr, and Hf) and V (i.e., Nb and Ta) metal atoms incorporated into the *BEA zeolite framework activate H_2O_2 to form a pool of hydroperoxide, peroxide, and superoxide intermediates. Time resolved UV−vis spectra acquired in situ during reaction of H_2O_2-activated materials with C_6H_{10} show that group IV metals react primarily through M-OOH/M-$(O_2)^{2-}$ (i.e., hydroperoxide/peroxide) intermediates, whereas M-$(O_2)^-$ (i.e., superoxide) complexes are the active intermediates on group V metals, which are further confirmed by the isomeric distributions of the epoxide products detected from reaction with *Z*-stilbene. The dependencies of turnover rates on reactant and product concentrations show that these group IV and V catalysts all irreversibly activate H_2O_2 to form a pool of M-(O_2) intermediates that react with C_6H_{10} or H_2O_2 via an Eley−Rideal mechanism to form $C_6H_{10}O$ or H_2O_2 decomposition products, respectively. Correlation of activation enthalpies for epoxidation and H_2O_2 decomposition to CD_3CN adsorption enthalpies reveal that stronger Lewis acids give greater turnover rates and selectivities toward olefin epoxidation. Additionally, activation enthalpies depend strongly on the energy of the LMCT band of the reactive intermediate for each M-β, which suggests that metals that more easily pull electron density from the bound dioxygen intermediates result in more electrophilic, reactive, and selective intermediates. As such, the design of catalysts with metal centers that are stronger Lewis acids can give both greater reactivity for olefin epoxidation and also greater selectivity and yield for these epoxidations on the basis of H_2O_2. Ongoing investigations in our group seek to understand the relationship between the electronic properties of the reactive intermediates and the steric or electronic properties of various olefins and how the energetics of epoxidation and related oxidation reactions is affected.

■ ASSOCIATED CONTENT

Supporting Information

The Supporting Information is available free of charge on the ACS Publications website at DOI: 10.1021/jacs.7b01422.

Characterization data, in situ spectroscopic data and processing, and activation enthalpy and entropy determination (PDF)

■ AUTHOR INFORMATION

Corresponding Author

*dwflhrty@illinois.edu

ORCID

Daniel T. Bregante: 0000-0003-2157-1286

Notes

The authors declare no competing financial interest.

■ ACKNOWLEDGMENTS

We thank Megan Witzke, Neil Wilson, and Pranjali Priyadarshini for insightful discussions, and Dr. Damien Guironnet for helpful discussions and use of lab equipment. D.T.B. was supported by the Department of Defense (DoD) through the National Defense Science & Engineering Graduate Fellowship (NDSEG) Program. This work was carried out in part in the Frederick Seitz Materials Research Laboratory Central Research Facilities at the University of Illinois. This material is based upon work supported in part by the U.S. Army Research Office under Grant W911NF-16-1-0128 and the National Science Foundation under Grant CBET-1553137.

■ REFERENCES

(1) Czako, B.; Kurti, L. *Strategic Applications of Named Reactions in Organic Synthesis*; Academic Press, 2005.
(2) Choi, W. J.; Choi, C. Y. *Biotechnol. Bioprocess Eng.* **2005**, *10*, 167−179.
(3) Lehmhus, D.; Busse, M.; Herrmann, A.; Kayvantash, K. *Structural Materials and Processes in Transportation*; Wiley-VCH: Germany, 2013.
(4) Wilson, N. M.; Bregante, D. T.; Priyadarshini, P.; Flaherty, D. W. *Catalysis* **2017**, *29*, 122−212.
(5) Epoxides. In *Ullmann's Encyclopedia of Industrial Chemistry*; Wiley-VCH: Weinheim, Germany, 2012.
(6) Ethylene Oxide. In *Ullmann's Encyclopedia of Industrial Chemistry*; Wiley-VCH: Weinheim, Germany, 2012.
(7) *Process Analyzers in Ethylene Oxide Production Plant*; Siemens, 2003.
(8) Linic, S.; Barteau, M. A. *J. Am. Chem. Soc.* **2003**, *125*, 4034−4035.
(9) Wen, C.; Yin, A.; Dai, W.-L. *Appl. Catal., B* **2014**, *160*−*161*, 730−741.
(10) Obama, B. *Science* **2017**, *355*, 126.
(11) Campos-Martin, J. M.; Blanco-Brieva, G.; Fierro, J. L. *Angew. Chem., Int. Ed.* **2006**, *45*, 6962−6984.
(12) Gleeson, D.; Sankar, G.; Catlow, R. A.; Catlow, C.; Meurig Thomas, J.; Spanó, G.; Bordiga, S.; Zecchina, A.; Lamberti, C. *Phys. Chem. Chem. Phys.* **2000**, *2*, 4812−4817.

DOI: 10.1021/jacs.7b01422
J. Am. Chem. Soc. XXXX, XXX, XXX−XXX

(13) Carati, A.; Flego, C.; Previde Massara, E.; Millini, R.; Carluccio, L.; Parker, W. O.; Bellussi, G. *Microporous Mesoporous Mater.* **1999**, *30*, 137−144.
(14) Park, S.; Cho, K. M.; Youn, M. H.; Seo, J. G.; Baeck, S.-H.; Kim, T. J.; Chung, Y.-M.; Oh, S.-H.; Song, I. K. *Catal. Lett.* **2008**, *122*, 349−353.
(15) Bregante, D. T.; Priyadarshini, P.; Flaherty, D. W. *J. Catal.* **2017**, *348*, 75−89.
(16) Ruddy, D. A.; Tilley, T. D. *J. Am. Chem. Soc.* **2008**, *130*, 11088−11096.
(17) Thornburg, N. E.; Nauert, S. L.; Thompson, A. B.; Notestein, J. M. *ACS Catal.* **2016**, *6*, 6124−6134.
(18) Cordeiro, P. J.; Guillo, P.; Spanjers, C. S.; Chang, J. W.; Lipschutz, M. I.; Fasulo, M. E.; Rioux, R. M.; Tilley, T. D. *ACS Catal.* **2013**, *3*, 2269−2279.
(19) Tang, B.; Dai, W.; Sun, X.; Guan, N.; Li, L.; Hunger, M. *Green Chem.* **2014**, *16*, 2281−2291.
(20) Cordeiro, P. J.; Tilley, T. D. *Langmuir* **2011**, *27*, 6295−6304.
(21) Guo, Y.; Solovyov, A.; Grosso-Giordano, N. A.; Hwang, S.-J.; Katz, A. *ACS Catal.* **2016**, *6*, 7760−7768.
(22) Ouyang, X.; Hwang, S.-J.; Xie, D.; Rea, T.; Zones, S. I.; Katz, A. *ACS Catal.* **2015**, *5*, 3108−3119.
(23) Thornburg, N. E.; Thompson, A. B.; Notestein, J. M. *ACS Catal.* **2015**, *5*, 5077−5088.
(24) Srinivas, D.; Manikandan, P.; Laha, S. C.; Kumar, R.; Ratnasamy, P. *J. Catal.* **2003**, *217*, 160−171.
(25) Lin, W.; Frei, H. *J. Am. Chem. Soc.* **2002**, *124*, 9292−9298.
(26) Clerici, M. G.; Ingallina, P. *J. Catal.* **1993**, *140*, 71−83.
(27) Kulkarni, B. S.; Krishnamurty, S.; Pal, S. *J. Mol. Catal. A: Chem.* **2010**, *329*, 36−43.
(28) Li, Y.-P.; Head-Gordon, M.; Bell, A. T. *ACS Catal.* **2014**, *4*, 1537−1545.
(29) Yang, G.; Zhou, L.; Han, X. *J. Mol. Catal. A: Chem.* **2012**, *363*−*364*, 371−379.
(30) Luo, H. Y.; Lewis, J. D.; Roman-Leshkov, Y. *Annu. Rev. Chem. Biomol. Eng.* **2016**, *7*, 663−692.
(31) Boronat, M.; Corma, A.; Renz, M.; Viruela, P. M. *Chem. - Eur. J.* **2006**, *12*, 7067−7077.
(32) Sastre, G.; Corma, A. *Chem. Phys. Lett.* **1999**, *302*, 447−453.
(33) Jenzer, G.; Mallat, T.; Maciejewski, M.; Eigenmann, F.; Baiker, A. *Appl. Catal., A* **2001**, *208*, 125−133.
(34) Bonino, F.; Damin, A.; Bordiga, S.; Lamberti, C.; Zecchina, A. *Langmuir* **2003**, *19*, 2155−2161.
(35) Boronat, M.; Concepción, P.; Corma, A.; Renz, M.; Valencia, S. *J. Catal.* **2005**, *234*, 111−118.
(36) Boronat, M.; Concepción, P.; Corma, A.; Navarro, M. T.; Renz, M.; Valencia, S. *Phys. Chem. Chem. Phys.* **2009**, *11*, 2876−2884.
(37) Lane, B. S.; Burgess, K. *Chem. Rev.* **2003**, *103*, 2457−2473.
(38) Wolf, P.; Hammond, C.; Conrad, S.; Hermans, I. *Dalton Trans.* **2014**, *43*, 4514−4519.
(39) Dzwigaj, S.; Millot, Y.; Méthivier, C.; Che, M. *Microporous Mesoporous Mater.* **2010**, *130*, 162−166.
(40) Vega-Vila, J. C.; Harris, J. W.; Gounder, R. *J. Catal.* **2016**, *344*, 108−120.
(41) Harris, J. W.; Cordon, M. J.; Di Iorio, J. R.; Vega-Vila, J. C.; Ribeiro, F. H.; Gounder, R. *J. Catal.* **2016**, *335*, 141−154.
(42) Escobedo Morales, A.; Sanchez Mora, E.; Pal, U. *Rev. Mex. Fis. E* **2007**, *53*, 18−22.
(43) International Zeolite Association: Verified Syntheses of Zeolitic Materials: Characterization by IR Spectroscopy. http://www.iza-online.org/synthesis/VS_2ndEd/IR_Spectroscopy.htm (accessed October 12, 2016).
(44) Roy, S.; Bakhmutsky, K.; Mahmoud, E.; Lobo, R. F.; Gorte, R. J. *ACS Catal.* **2013**, *3*, 573−580.
(45) Sushkevich, V. L.; Vimont, A.; Travert, A.; Ivanova, I. I. *J. Phys. Chem. C* **2015**, *119*, 17633−17639.
(46) Wang, J.; Kispersky, V. F.; Nicholas Delgass, W.; Ribeiro, F. H. *J. Catal.* **2012**, *289*, 171−178.
(47) Mahmoud, E.; Yu, J.; Gorte, R. J.; Lobo, R. F. *ACS Catal.* **2015**, *5*, 6946−6955.
(48) Daniell, W.; Topsøe, N. Y.; Knözinger, H. *Langmuir* **2001**, *17*, 6233−6239.
(49) Tang, B.; Dai, W.; Wu, G.; Guan, N.; Li, L.; Hunger, M. *ACS Catal.* **2014**, *4*, 2801−2810.
(50) Sushkevich, V. L.; Palagin, D.; Ivanova, I. I. *ACS Catal.* **2015**, *5*, 4833−4836.
(51) Madon, R. J.; Boudart, M. *Ind. Eng. Chem. Fundam.* **1982**, *21*, 438−447.
(52) Shetti, V. N.; Manikandan, P.; Srinivas, D.; Ratnasamy, P. *J. Catal.* **2003**, *216*, 461−467.
(53) Brutchey, R. L.; Ruddy, D. A.; Andersen, L. K.; Tilley, T. D. *Langmuir* **2005**, *21*, 9576−9583.
(54) Morlanés, N.; Notestein, J. M. *Appl. Catal., A* **2010**, *387*, 45−54.
(55) Chen, C.; Yuan, H.; Wang, H.; Yao, Y.; Ma, W.; Chen, J.; Hou, Z. *ACS Catal.* **2016**, *6*, 3354−3364.
(56) Yoon, C. W.; Hirsekorn, K. F.; Neidig, M. L.; Yang, X.; Tilley, T. D. *ACS Catal.* **2011**, *1*, 1665−1678.
(57) Bravo-Suárez, J. J.; Bando, K. K.; Lu, J.; Haruta, M.; Fujitani, T.; Oyama, S. T. *J. Phys. Chem. C* **2008**, *112*, 1115−1123.
(58) Ziolek, M.; Sobczak, I.; Decyk, P.; Sobańska, K.; Pietrzyk, P.; Sojka, Z. *Appl. Catal., B* **2015**, *164*, 288−296.
(59) Ziolek, M.; Sobczak, I.; Decyk, P.; Wolski, L. *Catal. Commun.* **2013**, *37*, 85−91.
(60) Bonino, F.; Damin, A.; Ricchiardi, G.; Ricci, M.; Spano, G.; D'Aloisio, R.; Zecchina, A.; Lamberti, C.; Prestipino, C.; Bordiga, S. *J. Phys. Chem. B* **2004**, *108*, 3573−3583.
(61) Wang, L.; Xiong, G.; Su, J.; Li, P.; Guo, H. J. *J. Phys. Chem. C* **2012**, *116*, 9122−9131.
(62) Notari, B. *Adv. Catal.* **1996**, *41*, 253−334.
(63) Sams, C. K.; Jørgensen, K. A. *Acta Chem. Scand.* **1995**, *49*, 839−847.
(64) Raj, N. K. K.; Ramaswamy, A. V.; Manikandan, P. *J. Mol. Catal. A: Chem.* **2005**, *227*, 37−45.
(65) Bordiga, S.; Damin, A.; Bonino, F.; Ricchiardi, G.; Lamberti, C.; Zecchina, A. *Angew. Chem., Int. Ed.* **2002**, *41*, 4734−4737.
(66) Pauling, L. *J. Am. Chem. Soc.* **1932**, *54*, 3570−3582.
(67) Rohrer, G. S. *Structure and Bonding in Crystalline Materials*; Cambridge University Press, 2001.
(68) Anslyn, E. V.; Dougherty, D. A. *Modern Physical Organic Chemistry*; University Science, 2005.
(69) Clerici, M. G. *Kinet. Catal.* **2015**, *56*, 450−455.
(70) Gunther, W. R.; Michaelis, V. K.; Griffin, R. G.; Román-Leshkov, Y. *J. Phys. Chem. C* **2016**, *120*, 28533−28544.
(71) Tielens, F.; Shishido, T.; Dzwigaj, S. *J. Phys. Chem. C* **2010**, *114*, 3140−3147.
(72) Dzwigaj, S.; Millot, Y.; Che, M. *Catal. Lett.* **2010**, *135*, 169−174.
(73) Wang, Y.; Lewis, J. D.; Román-Leshkov, Y. *ACS Catal.* **2016**, *6*, 2739−2744.

DOI: 10.1021/jacs.7b01422
J. Am. Chem. Soc. XXXX, XXX, XXX−XXX